Mechanical and electrical characterization of resonant piezoelectric microbridges for strain sensing

M. Schlögl [*], S. Köpl, J. Hiesberger, M. Schneider, U. Schmid

TU Wien, Institute of Sensor and Actuator Systems, Gußhausstraße 27-29, E366, Vienna 1040, Austria

ARTICLE INFO

ABSTRACT

This work reports on a resonantly operated piezoelectric MEMS strain sensor based on a microbridge structure. The resonator is excited with a sputtered aluminum nitride layer and was fabricated with standard CMOS processing techniques. The mechanical frequency spectra and the mode shapes were studied with a laser Doppler vibrometer. Additionally, an electrical read out was realized by measuring the conductance spectra with an impedance analyzer. Several sensor devices varying in width have been fabricated and the differences in the resonance frequency, the mechanical displacement and the electrical conductance spectra have been evaluated, with a focus on the first two Euler-Bernoulli modes. The buckling behavior of the devices under high compressive external strain was analyzed. Furthermore, the mode veering phenomenon could be observed and is analyzed in detail. To classify this new type of strain sensor a frequency-dependent gauge factor has been defined. It shows that the sensor devices exhibit exceptionally high gauge factors, one to two orders of magnitude higher than conventional strain gauges based on the piezoresistive effect.

1. Introduction

The precise knowledge on the local strain distribution in mechanical structures and force-loaded systems requires most accurate and compact sensor elements to enable demanding surveillance and metrological applications such as structural health monitoring [1–3], tactile sensing for robotic systems [4–6] or wearable electronics [7–9]. Therefore, a lot of effort has been invested in the past to realize and evaluate the potential of different strain sensing mechanisms due to specific application-driven requirements. In the late 1930 s the bonded wire resistance strain gauge has been invented [10,11] and was the state-of-the-art strain measuring technique for many decades. Improvements have been achieved by introducing tailored materials and designs to overcome typical restrictions like a limited operational temperature range [12], a high cross-sensitivity to temperature [13,14] or the impact of parasitic effects like a high transverse strain sensitivity [15,16].

Semiconductor strain gauges based on the piezoresistive effects improved substantially the accuracy in local strain sensing due to an increased gauge factor (GF) of up to 200 [17,18] compared to 2–5 of pure metal foil strain gauges [17]. In contrast, optical strain gauges use fiber Bragg gratings to alter the refractive index of optical fibers which allows to block certain frequencies of the transmitted light spectrum. This modified light spectrum is depended on the strain applied to the fiber and therefore, this technique enables to sense mechanical strain [19]. Due to the low internal losses and the possibility to fabricate long optical fibers with high precision this technique is most beneficially applied to large structures having dimensions up to several kilometers. Furthermore, they are insensitive to interfering electrical fields and immune to chemical corrosion making them most suitable for harsh environmental applications [20].

More exotic versions of strain gauge sensors are based on digital image correlation [21], electronic speckle pattern interferometry [22] or integrated optical ring resonators [23], just to mention a few most emerging technologies.

The recent rise of wireless sensor networks demands, however, reliable sensors with very low power consumption in the range of micro- or nano watts. Furthermore, longer lifetimes up to 20 years [24,25] are necessary especially for e.g. automotive and structural health monitoring applications. MEMS (micro electromechanical systems) sensors offer a most excellent technology platform to fulfill both key requirements. Due to their small size, they can be designed for extremely low operation voltages and therefore exceptionally low power consumptions. Typically, they are fabricated in CMOS compatible silicon

---

* Corresponding author.
E-mail address: matthias.schloegl@tuwien.ac.at (M. Schlögl).

micromachining.

The last decade showed a strong trend towards piezoelectric MEMS sensors, due to their compact design and their low power consumption. Most often they are operated in resonance, whereas the key mechanical building blocks for the resonating element are designed either as beams, cantilevers or plates. Furthermore, the piezoelectric transducer allows both to stimulate the mechanical resonance electrically and to read out electrically by recording the conductance spectrum. Specific resonances can be excited most efficiently depending on resonator design parameters, such as its length, thickness and mass [26], but also the electrode design [27] plays a crucial role. By tracking the change of resonance frequency or its quality factor the devices can be used to measure physical quantities, like viscosity of a liquid [28], mass of a particle [29] and much more. If those MEMS resonators are built in a double-clamped beam-like structure, also called microbridge, they can be used to sense axially applied strain [30–32]. The most common methods for electric actuation are by electrostatic forces, via capacitive structures [33,34] and by piezoelectric forces which in turn reduces the necessary high voltages associated with the prior mentioned transducer principle [13].

In this study, we evaluate a MEMS strain sensor of high responsivity, which is based on a piezoelectric resonant microbridge design offering an electrical read-out capability through conductance spectroscopy. Via laser Doppler vibrometry we give a detailed overview of the mechanical mode shapes and their vibrational displacement behavior under different axial mechanical loading conditions. Next, a concept to increase the electrical output signals is presented by increasing the microbridge width while leaving the original frequency characteristics unaffected. Additionally, the influence of curve veering and creeping due to the viscous behavior of the used adhesive on the frequency characteristics of the MEMS sensor is studied. Finally, a frequency dependent gauge factor is determined, and these values are benchmarked against the performance to state of the art resonant as well as non-resonant strain sensors.

2. Sensor design and fabrication

The MEMS sensor device in this work is based on a micromachined beam structure clamped on both ends, also called microbridge. It is operated as a resonator and is electrically excited with an integrated piezoelectric aluminum nitride thin film, shown in Fig. 1. Among other device as well as ambient-related parameters the resonance frequency spectrum of microbridge resonators depend on the intrinsic stress σ of the thin films and on the externally applied strain ε. Positive values of ε are associated with a longitudinal expansion of the structure which results in an increase in resonance frequencies independent of their specific mode, whereas negative values of ε lead to compression of the microbridge which results in a decrease in resonance frequencies. The latter statement only holds true, as long as the microbridge remains in a flat state. If the compressive stress exceeds a critical value, the microbridge starts to buckle. In this state, the resonance behavior is different

resulting in a distortion of the mode shapes, which will be discussed in the "Experimental Details" section.

The fabrication process shown in Fig. 1(a), is based on an SOI (silicon-on-insulator) wafer with a 2 μm device layer and a 400 μm handle layer, separated by a 0.5 μm thin buried oxide (BOX). The top surface of the wafer is passivated by a stress-compensated combination of 0.25 μm thermally oxidized SiO_2 followed by 0.08 μm of stochiometric Si_3N_4 synthesized by low-pressure chemical vapor deposition. The bottom electrode consists of a 0.18 μm thick gold electrode layer in combination with a 0.02 μm thick chromium thin film as adhesion promoter underneath, deposited by e-beam evaporation. The piezoelectric active material is made of 0.7 μm aluminum nitride sputter deposited by a "Von Ardenne" LS 730 S at 800 W of plasma power and 0.2Pa chamber pressure under pure nitrogen atmosphere. The sputter target was a 6" pure aluminum target and the substrate-target distance was 65 mm. Top and bottom electrodes are designed such that they cover the same AlN related area on the microbridge, thus forming a typical capacitive structure. Both electrodes were patterned with a standard lift-off process. The piezoelectric aluminum nitride layer was also patterned by a photoresist-based lift-off process, but with twice the thickness as for the electrode lift-off. Deep reactive ion etching was applied to pattern both the device and handle layer followed by a hydrofluoric acid dip to remove the BOX. The wafer was diced with a wafer saw and finally cleaned in acetone and isopropanol baths.

To investigate the influence of the width, microbridges with three different geometrical dimensions have been fabricated, as shown in Table 1.

Due to the intrinsic compressive stress which sputtered aluminum nitride thin films typically exhibit, the microbridges are buckled after the manufacturing process. The deflection shape due to buckling has been studied with a Fries Research Technology (FRT) MicroProf MPR 1261 white light interferometer and is shown in Fig. 2(a). Fig. 2(b) shows a deflection profile along the microbridges length and the maximum deflection can be measured to $D = 23.8\mu m$. The buckling could also be visualized with a Hitachi SU8030 scanning electron microscope (SEM) with an acceleration voltage of 5 kV and an emission current of 20 mA. Fig. 2(c) shows the microbridge after the manufacturing process in the buckled state, whereas in (d) the microbridge has been stretched to reach the non-buckled state, by pre-straining it during the mounting process as described in Section 4.5.
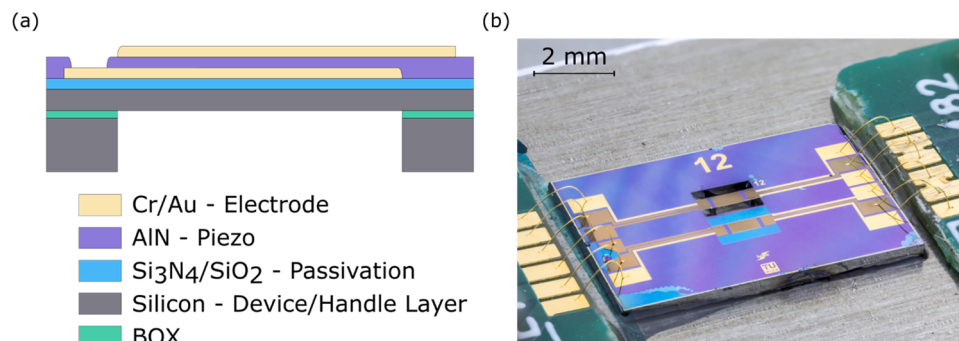
Table 1
Device dimensions with varying width.

Nr	Microbridge Dimensions
S1	1000x100x3 μm^3
S2	1000x200x3 μm^3
S3	1000x400x3 μm^3

Fig. 1. (a) Schematic cross-section of a microbridge-type resonant strain gauge sensor. (b) Optical micrograph of a glued and wire-bonded MEMS strain gauge sensor.
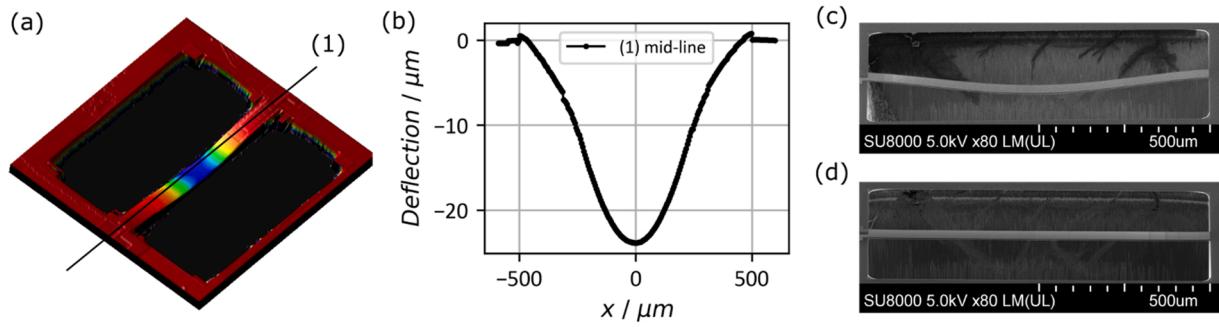
Fig. 2. 3-Dimensional view of a white light interferometer measurement of a buckled microbridge after fabrication in (a) and a deflection profile along the beam length in (b). SEM images of the same beam in a buckled state in (c) and in a non-buckled state in (d).

3. Experimental details

3.1. Measurement setup

The setup for measuring the strain sensors is schematically illustrated in Fig. 3(a). The frequency response was measured with two independent methods, optically and electrically. The displacement d and the mechanical mode shape of the microbridge were measured with a laser Doppler vibrometer (LDV, MSA-500) from Polytec, whereas the resonator was excited with a chirp signal with a bandwidth of 1 MHz and an amplitude of 100 mV. To record the mode shapes, a grid of scan points across the surface of the microbridge has been defined with a spacing of $18\mu m$ and $21\mu m$ in x- and y-direction, respectively. For each scan point a frequency dependent vibrational displacement is measured. All these individual data are then combined to the mode shapes with the software provided by the MSA-500. Important to note is that the LDV initially measures the velocity, from which the software then calculates the displacement. Therefore, it only gives information about the dynamic component of the displacement, ignoring the static deflection of the microbridge due to buckling.

The electrical conductance spectrum $G(f)$ was measured with a Zurich Instruments MFIA impedance analyzer (IA) while the sensor was excited with the built-in frequency generator providing a frequency sweep with a bandwidth of 1 MHz and a voltage amplitude of 100 mV.

To determine the natural resonance frequency f_0 from the optical LDV measurements the fitting function $D_{fit}(f)$ from Eq. (1) was used, which represents the displacement amplitude for a harmonic oscillator [35].

$$D_{fit}(f) = \frac{D_0}{4\pi^2 \sqrt{4\zeta^2 f_0^2 f^2 + (f_0^2 - f^2)^2}} \tag{1}$$

The parameter ζ represents the damping coefficient which can be used to calculate the quality factor using Eq. (2) and D_0 represents the maximum amplitude.

$$Q = \frac{\sqrt{1 - 2\zeta^2}}{2\zeta} \tag{2}$$

The conductance from the electrical measurements has been fitted with $G_{fit}(f)$ from Eq. (3), derived from a standard series LCR resonant circuit.

$$G_{fit}(f) = \frac{G_0}{1 + \frac{1}{4\xi^2}\frac{f_0^2}{f^2}\left(\frac{f^2}{f_0^2} - 1\right)^2} \tag{3}$$

The parameter ξ represents the damping coefficient and G_0 the conductance amplitude at $f = f_0$. Since Eqs. (1) and (3) describe the same mechanical system, both damping parameters are identical in the absence of noise and measurement related drifts, thus $\zeta = \xi$. The quality factor of the conductance resonance peak can then be calculated with:

$$Q = \frac{\sqrt{1 - 2\xi^2}}{2\xi} \tag{4}$$

Both fitting functions are plotted in Fig. 3(b) and (c) fitted on representative resonance curves for the displacement and for the conductance, whereas the conductance was related to the angular frequency $\omega = 2\pi f$ for better comparability over a wide range of
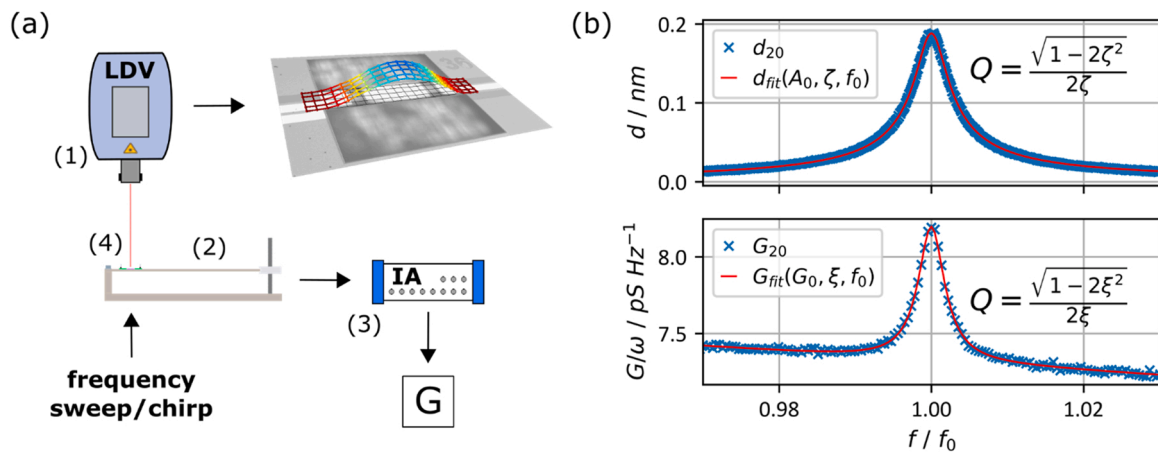

Fig. 3. (a) Measurement setup to characterize the displacement d and the mode shape of the resonant MEMS strain sensors with the laser Doppler vibrometer (LDV). The electric response represented by the conductance $G(f)$ and the susceptance $B(f)$ is recorded with the impedance analyzer (IA). A chirp signal provided by the built-in frequency generators was used to excite the strain sensor. In (b) and (c) are measurement data and corresponding fitted Functions $D_{fit}(f)$ for the displacement spectrum and $G_{fit}(f)$ for the conductance spectrum, respectively.

frequencies.

The precision of f_r obtained by ten repetitive measurements lies within 0.02% and for the displacement d within 2.5% for both the electrical and the optical measurements, after an initial waiting period of 15min to minimize the influence of creeping, as explained in Section 4.2.

To apply mechanical strain in a defined and reliable way with different values to the resonant strain sensor, a custom-built measurement setup was designed consisting of a deflectable cantilever made of aluminum (Al), shown in Fig. 4(a). Fig. 4(b) shows a schematic overview with the sensor device (1) and its connecting PCBs (2) glued onto the Al cantilever (3). The tip of the cantilever was displaced by a stepper motor (4) of the type Stepperonline Nema 17 with a spindle (5) which has a pitch of 1 mm rev^{-1}. The stepper motor was controlled by an Arduino Mega with a motor driver board (6) and provided a resolution for the spindle of 0.05 revolutions translating to 50μm for the tip displacement of the cantilever.

Based on the thickness h_C, the sensor thickness h_S (including device layer, electrodes and the piezoelectric layer), the length L of the cantilever and the tip displacement d_C of the cantilever the strain sensor can be exposed to a certain strain ε_x at the position x_0 depending on the local distribution of the latter parameter on the cantilever surface. It can be calculated by the Euler-Bernoulli beam equations [36] in general to

$$\varepsilon_x = -3 \frac{d_C z}{L^3}(L-x), \tag{5}$$

whereas z is the distance from the neutral axis to the point of interest and x is the distance from the clamping point of the cantilever. They can be expressed with

$$x = x_0, \quad z = h_C/2 + h_S, \tag{6}$$

which then leads to the strain at the position of the MEMS sensor

$$\varepsilon_x = -\frac{3}{2} \frac{d_C(h_C + 2h_S)}{L^3}(L - x_0) \tag{7}$$

Fig. 4(c) shows the strain dependent on the sensor position along the cantilever for three different maximum tip displacements d_C. If the cantilever is bent down the sensor is stretched, resulting in positive values for epsilon and vice versa. Fig. 4(d) shows the strain dependence on the tip displacement for three different sensor positions. The closer the sensor is mounted to the fixed cantilever base ($x = 0$), the more strain is applied to the sensor. As the whole strain sensor chip including contact pads is 7.5 mm long, the minimal sensor position measured from

the base of the cantilever is half the chip length, therefore 3.75 mm and the maximal position is about 196 mm. The distance chosen for further characterizations in this work was 25 mm (orange curve in Fig. 4(d)), which leaves enough space for connecting the PCBs for electrical read-out.

The strain sensor was glued at an elevated temperature of 120 °C for 20 min with a two-component epoxy raisin EC101 from Polytec onto the aluminum cantilever. The pads of the device were connected with wire bonds to PCBs, which provide connectors for the measurement devices.

4. Results and discussion

Typical frequency responses for both detection schemes (i.e. optical and electrical) are displayed in Fig. 5(a). For the LDV measurements the frequency response from one single device is the averaged response across all surface scan points. Doing so, the displacement is plotted as an averaged value instead of the maximum displacement, which would be presented when reporting the results of single point measurements. The reason for this will be explained when the mode shapes and displacements are discussed in more detail.

Depending on the polarization direction of the applied electrical field at each electrode, depicted in Fig. 5(b) certain mode shapes $\phi(x)$ are excited more efficiently than others. For symmetrically polarized electrodes, the excitation of even modes such as 20 and 40 is preferred, for which applies $\phi(x) = \phi(-x)$. They feature an even number of nodal lines along the width of the microbridge and are plotted in red for the LDV and in dark blue for the IA measurements. For antisymmetrically polarized electrodes, the odd modes like 30 and 50, for which applies in contrast to the previous $\phi(-x) = -\phi(x)$. Those modes feature an odd number of nodal lines along the width and are plotted in orange for the LDV and light blue for the IA measurements.

Using the strain characterization setup, both the frequency response and the modification of the original mode shape were measured as a function of strain broad range of strain values. Fig. 6(a) shows the averaged mechanical displacements d_a for the resonance peak of the 20-mode. As expected, not only the resonance frequency depends on the applied strain, but also the peak height. Next, the resonance frequency values are plotted as a function of the applied strain ε, as yielded in Fig. 6 (b) which also includes illustrations of selected mode shapes.

To start, it is important to note that for the frequency curve of all even modes, there exists a characteristic strain value where the resonance frequency reaches a minimum. At this critical strain value ε_c, the microbridge changes from a buckled to a non-buckled state. ε_c is therefore labeled as buckling point. We normalized the plot so that $\varepsilon = 0$
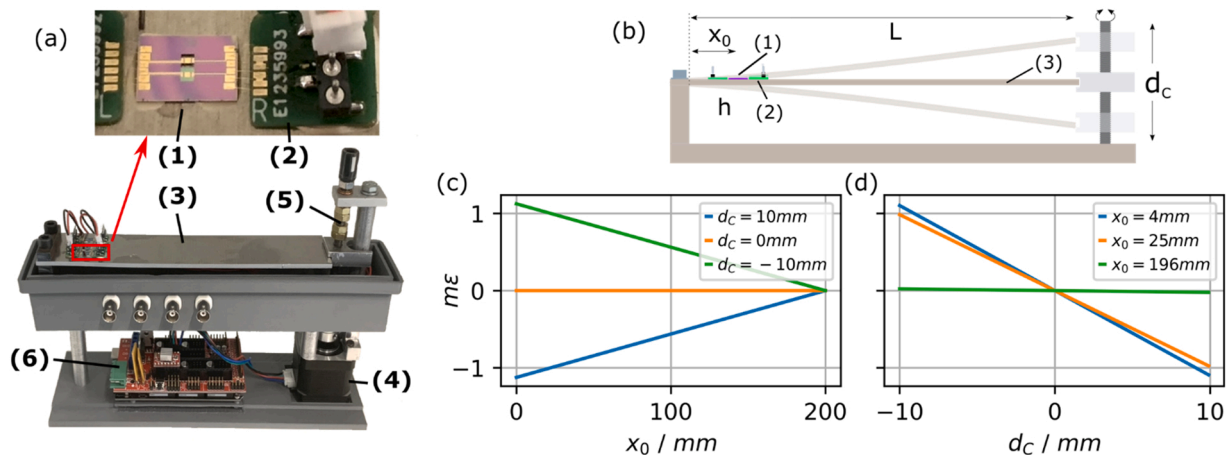

Fig. 4. (a) Optical photograph of the custom-made strain characterization setup with (1) the sensor device, (2) the connecting PCBs and (3) the measurement cantilever, (4) the stepper motor connected to (5) the spindle and (6) the controller consisting of an Arduino Mega with a motor driver board. (c) Correlation between mechanical strain at the sensor position x for different maximum tip displacements d_0 of the cantilever. (d) Correlation between mechanical strain and tip displacement for various sensor positions x_0.
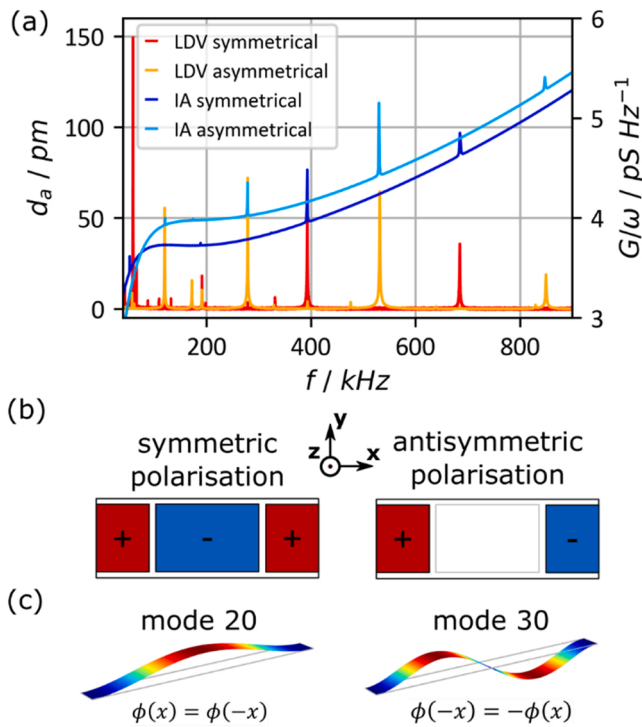
Fig. 5. (a) Resonance responses for a resonantly operated microbridge-type strain sensor measured optically and electrically in two different electrode configurations. (b) Electrode configurations for a symmetric and antisymmetric polarization of the applied electrical field and (c) their according mode shapes.

The quality factors of all modes were determined by using Eq. (2) with the damping coefficient attained from the fit in Eq. (1). The frequency responses were analyzed at a strain value close to the buckling point and far away from any curve veering transition zones, otherwise the signal strength is either too low to reasonable fit the data or the resonance peaks show non-linear effects. All modes exhibit reasonable Q-values between 200 and 400 being in excellent agreement with those reported in literature [13,37] for microbridge type resonators in air. Detailed values can be taken from Table 2.

Bouwstra et al. [38] studied the resonance frequency spectra of strained micromachined clamped-clamped beam structures. They started with both flat and initially buckled microbridges and investigated the behavior of the first and second flexural as well as of the first torsional mode, respectively. Starting from the general Euler-Bernoulli beam theory they developed an expression to estimate the resonance frequencies in the buckling and the non-buckling regime. They found out, that while the even 20-modes resonance frequency changes in the buckling regime, the odd 30-mode is not affected by the buckling induced strain. They explained this with the orthogonality between the symmetric deflection shape of the buckling and the anti-symmetric vibration shape.

Another type of modes are torsional modes which contain one or more nodal lines along the length of the microbridge. Torsional modes can also be classified into even and uneven modes, with the same behavior as their non-torsional counterpart. They are less suitable for strain sensing as shown below but are discussed for the sake of completeness.

is at this buckling point. For these types of modes, the frequency increases when enhancing the strain above ε_c.

The other type of modes are odd modes, which show increasing resonance frequencies for $\varepsilon > \varepsilon_c$, but almost constant f values for $\varepsilon < \varepsilon_c$.

Fig. 6(c) shows f as a function of ε for the first two flexural modes in more detail, measured with the LDV (blue and orange curve) and with the IA (green and red crosses). Again, both measurement approaches fit very well together and show that both techniques give very similar results.

Table 2

Q-factors of modes 20–60 for all three devices.

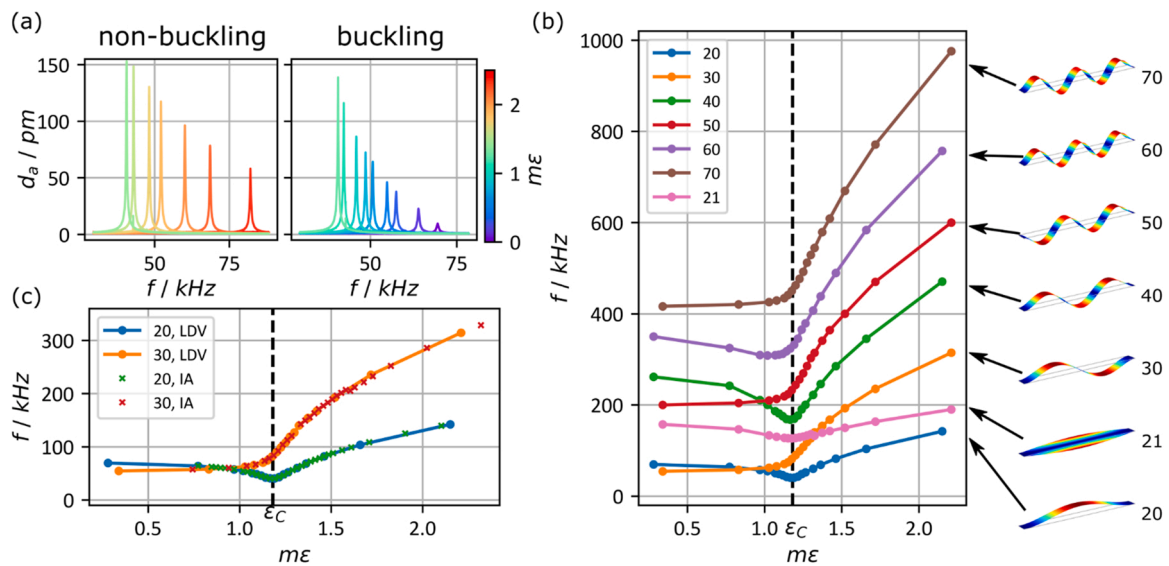| Mode	Q-Factor / LDV		
	S1	S2	S3
20	230	239	218
30	261	269	218
40	200	235	205
50	208	188	248
60	246	291	315

Fig. 6. (a) The vibrational displacement around the resonance frequency for the 20-mode for different strain values in the buckling regime and the non-buckling regime. (b) All resonance frequencies as a function of the applied strain measured with the LDV. (c) Comparison of the change in the resonance frequency for a MEMS strain sensor measured with LDV and IA in the two electrode configurations.

4.1. Mechanical deflection and mode shape

As already noticeable in Fig. 6(a) the height of the resonance peaks changes depending on the applied strain. Fig. 7(a) shows the peak maxima $d_{a,max}$ of the averaged frequency spectra for the modes 20 and 30. The x-axes in the following plots have been normalized such that the critical strain ε_c is at $\varepsilon = 0$. This makes it possible to define two different regimes, depending on whether the microbridge is buckled or not. In the latter regime both modes show a similar decaying amplitude with increased strain. In the buckled regime, however, the mode shapes measured by the LDV are distorted (Fig. 7(c)) and can only be interpreted when the buckling is superposed to the measurement, shown in Fig. 7(d). This distorted mode shape also makes it obvious why the averaged amplitude over the whole measured surface gives a better understanding of the general behavior of the displacement than a single point measurement. While the amplitude of the resonance peak for the 20-mode decreases quickly with increasing compressive strain, the 30-mode is less affected.

This behavior has already been observed in experimental studies in several publications [39–41]. Nayfeh et al. [42] developed an analytical expression to estimate the form of the mode shapes depended on the buckled deflection. They showed that even mode shapes are distorted, while odd mode shapes are not affected by the buckling. However, our measurements show that if strain exceeds a certain value – in this case $-0.5m\varepsilon$ – then the odd mode shapes also get distorted which also explains the decrease in the amplitude for very high negative strain values (see point 4 in Fig. 7).

Important to note is that the initial deflection due to buckling reaches several micro-meters, while vibrational displacements are in the pico-meter range. Therefore, in Fig. 7(d) the buckling deflection has been scaled down to give a qualitative view on the vibrational behavior in the buckling regime.

4.2. Influence of adhesive

A common method to mount metallic foil-type strain gauges to the device under test is by inserting an adhesive between the sensor and the underlying surface, respectively. Because of the strong difference in elasticity of the adhesive in comparison to the sensor device materials as well as the specimen a creeping effect can occur which changes the transferred strain characteristics over time. Fig. 8(a) shows the resonance frequency of sensor device S1 for five different applied external strain values. The given strain value is then kept constant for $15min$ and afterwards the strain is reverted back to the initial value and again kept constant for $15min$. After an initial frequency jump of Δf_ε the resonance frequency drifts slowly back of about Δf_C due to creeping resulting from the viscoelastic nature of the polymer-based adhesive. This behavior can be described by Burger's mechanical model, which usually describes the time dependent strain behavior of a material under stress [43,44]. It consists of a static component ε_s, a time dependent linear component $\varepsilon_l(t)$ and a time dependent, exponentially decaying component $\varepsilon_e(t)$ shown in Eq. (4).

$$\varepsilon = \varepsilon_s + \varepsilon_l(t) + \varepsilon_e(t) \tag{8}$$

Fig. 8(b) shows the frequency shift Δf_C due to creeping without the frequency shift Δf_ε originating from the externally applied strain. If we compare the graph to the model in Eq. (4) we have to consider that creeping of the adhesive is relaxing the strain transferred to the specimen, thus reducing the nominal mechanical load. Comparable to the adhesive the measured frequency shift can be described by three components: a static, a time dependent linear and a time dependent exponential component, as given in Eq. (5).

$$\Delta f_C = \Delta f_{C,s} + \Delta f_{C,l}(t) + \Delta f_{C,e}(t) = \Delta f_{C,s} + lt + d + e_1 \bullet \exp(e_2 t) \tag{9}$$

The value of $\Delta f_{C,s}$ cannot be evaluated as it is not possible to distinguish it from Δf_ε generated by the externally applied strain. The inset in Fig. 8(b) shows a representation of the time dependent components for one curve and the model with fitted parameters l, d, e_1, e_2, indicating that our adhesive is well represented by Burger's Model. This creeping behavior influences the frequency measurements and cannot be easily compensated as the strain and creep history of a polymer-based adhesive is included in its actual behavior. Nevertheless, if we compare Δf_C to Δf_ε and estimate the reduction in responsivity for the sensor device we obtain a value of $1-2\%$ plus the reduction due to the static component of the creep $\Delta f_{C,s}$.

In order to achieve a better reproducibility in the frequency domain, we estimated the dwell time to stabilize $\Delta f_{C,e}(t)$ to about $600s$ per $1m\varepsilon$ of applied strain before starting a mechanical load measurement.
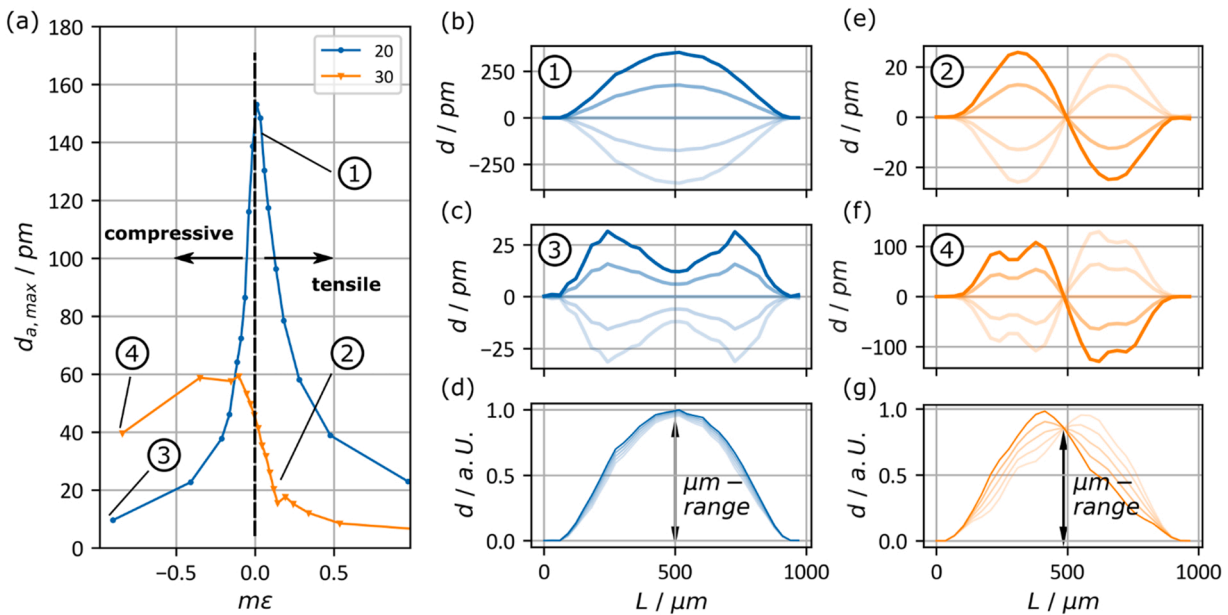

Fig. 7. (a) Averaged mechanical displacement d_a over applied strain for the 20 and 30-mode, (b) mode shape of the 20-mode at the buckling point, (c) in the compressively stressed regime at $\varepsilon = -0.9$ mm m^{-1} but below the critical stress value causing buckling and (d) in the buckled regime, meaning above the critical stress value causing buckling of the microbridge. (e-g) Mode shapes of the 30-mode under the same circumstances as in (b-d).
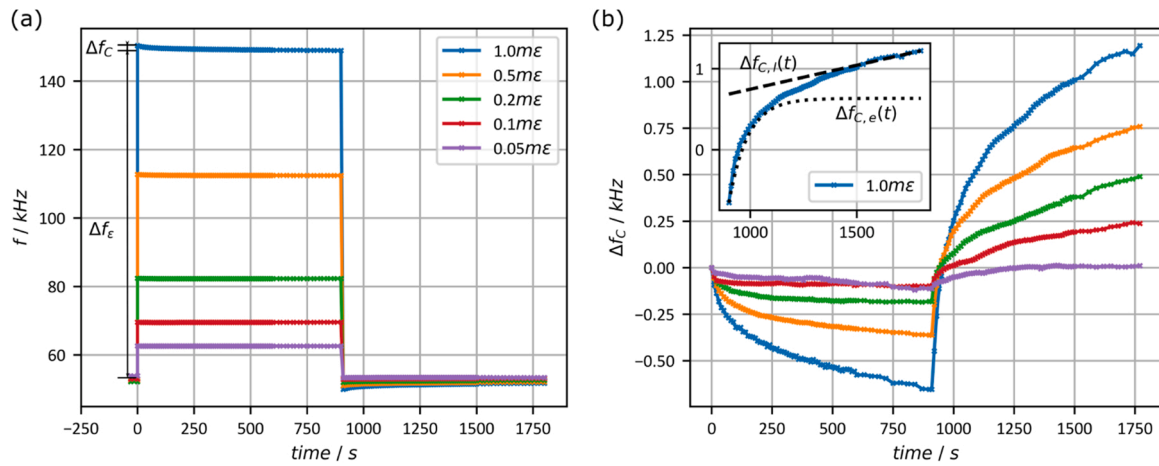
Fig. 8. Resonance frequency of the first flexural mode over time for five different applied strain values. (b) Frequency shift of sensor device S1 over time due to creeping arising from the high elasticity of the adhesive for five different applied strain values.

Methods to reduce the influence of creeping range from decreasing the overall thickness of the sensor device by polishing the handle layer of the SOI wafer [45] to the substitution of the polymer based adhesive through an eutectic bonding process [46]. Both methods do not only reduced creeping, but also showed increased reliability due to a better match between the stiffness of the sensor material and the adhesion layer, respectively.

4.3. Curve veering

Another effect coming into play is when the resonance frequencies of different modes get shifted in a way that they seemingly cross-over. But instead of crossing they veer away, so that this phenomenon is called curve veering or avoided crossing [47]. The region where those modes veer is typically referred to as "transition zone" [48]. Several publications have experimentally validated the curve veering effect for microbridge type resonators [49–52], but it also has been shown for other resonator designs [53,54].
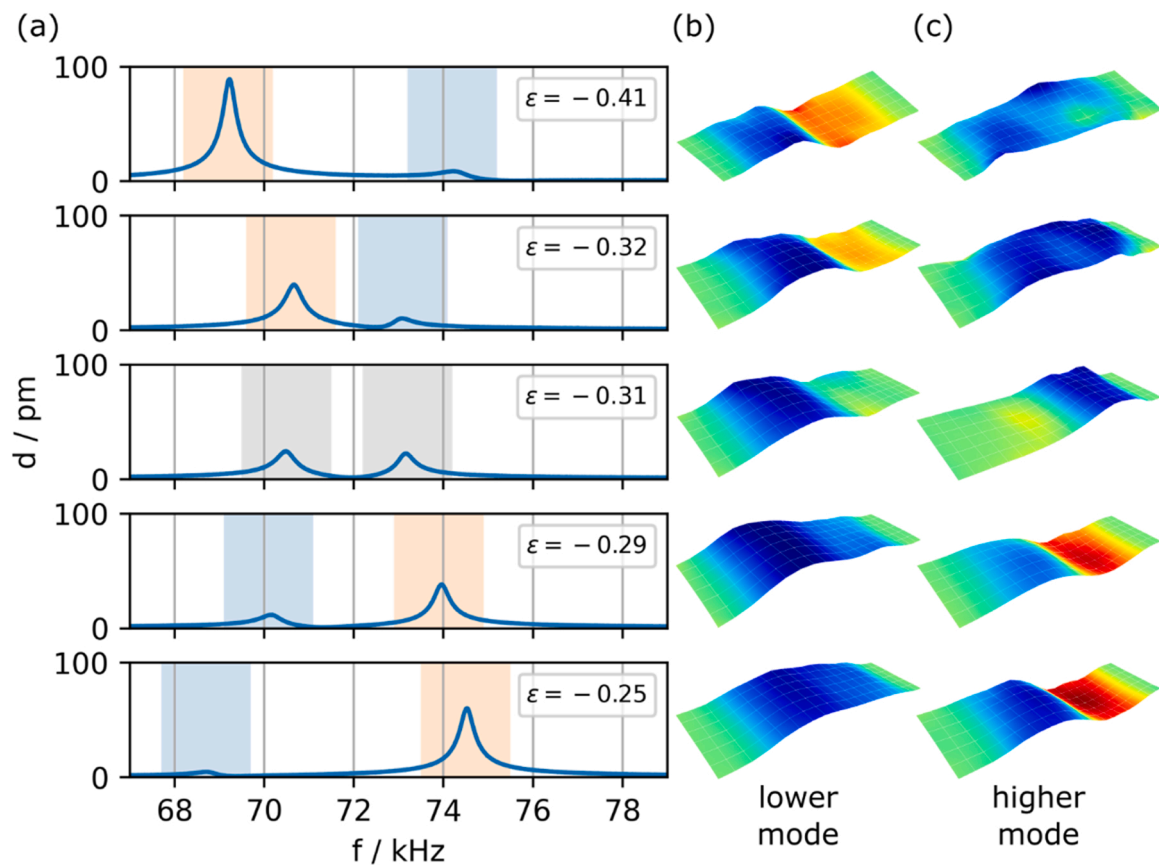

Fig. 9. (a) Frequency spectra of a microbridge for five different strain values showing the resonances of the 20 (marked in blue) and 30 (marked in orange) mode around their veering point. The areas marked in gray show mode shapes where a clear assignment to a certain mode is not possible, due to the mixing of the two mode shapes. (b) Mode shapes measured with the LDV of the lower resonance and (c) of the higher resonance.

Fig. 9(a) shows the frequency response for 5 different strain values, covering the modes 20 and 30 of a device with dimensions of $1000x400x3\mu m$, in an antisymmetric electrode configuration. In contrast to the previous measurements the displacement d in Figs. 9 and 10 was measured at a single scan point giving absolute values. The modes 20 and 30 are highlighted in blue and orange, respectively. Fig. 9 (b) shows the measured mode shape of the lower, whereas Fig. 9(c) the mode shape of the higher resonance peak, respectively. Obviously, the mode shapes change depending on the strain and on the distance in frequency of the two resonance peaks. In the transition zone the mode shapes are distorted and cannot be related to any mode numbering, indicated with gray highlighting.

Fig. 10 (a) shows the resonance frequency as a function of the applied strain for both modes again. The mode shapes are indicated by the blue and orange areas for the modes 20 and 30, respectively. The gray and black curves are the actual measured resonance peaks. As explained before, they approach each other, but instead of crossing they veer away and exchange their mode shape. Fig. 10 (b) shows the maximum values for the displacement of the two modes and it is obvious that the modes not only exchange their shape but also their amplitudes.

When this device concept is exploited as strain sensor, curve veering might affect the accuracy of the measurement results in these transition zones in two ways. First, the wrong mode can be followed when crossing the transition zone, which would lead to false result interpretations e.g., decreasing instead of increasing frequency with increasing strain, as shown in Fig. 10 (a) for mode 30 (orange area). Second, when following the correct mode, a jump has to occur from one mode to the other, leading to higher and difficult to predict values of the responsivity. A simple possibility to avoid both cases is to define a working point in the frequency spectrum which avoids any transition zones. Another approach is to simultaneously measure the resonance frequency and its amplitude, as this changes together with the mode shape. In this case, the mode with the higher amplitude (i.e. mode 30) would be the mode of choice, as depicted in Fig. 10 (b).

4.4. Influence of microbridge width

Fig. 11 (a-d) shows the frequency as a function of strain for the modes 20, 30, 21 and 31 for microbridges with widths of $100\mu m$, $200\mu m$ and $400\mu m$. Within the usual approximation for the EBT of a long thin and slender beam, the resonance frequencies for the out of plane modes, with no nodal lines along the beam length are independent from the width of the beam.

For the modes 20 and 30 in the non-buckled regime the different microbridges show similar frequency curves. The small variations can be traced back to inaccuracies in the manufacturing process. Especially the thickness of the sputtered aluminum nitride thin film plays a huge role, as the intrinsic stress typically decreases with increasing thickness [55].

In the buckling regime the 20-mode differs a lot for the three different widths, while for the 30-mode the frequency curves match well. Bouwstra et al. showed that one of the reasons for the behavior is the initial deflection of the microbridge [38].

The resonance frequencies of the torsional modes 21 and 31 additionally depend on the beam's width. As this kind of modes are not covered by the Euler Bernoulli beam equations, which are based on a long, thin and slender beam we can only give a qualitative description of their behavior.

The frequency curve exhibits a smaller slope than their non-torsional counter parts making them less sensitive to strain. The curve is also shifted along the y axis, depending on the width of the microbridge. Higher widths result in a negative shift, bringing the torsional modes closer to their non-torsional pendant without crossing it e.g., the 21-mode closer to the 20-mode, seen in Fig. 11 (c-d). The 31-mode for the microbridge with a width of $100\mu m$ could not be measured due to the weak signal strength and is therefore missing in Fig. 11 (d). The width dependence of these Kirchhoff-love modes was also found in cantilever type resonators with varying width [26] with a similar behavior.

Fig. 12 (a) and (b) show the displacement amplitude measured with the LDV as a function of strain in the resonance case for the 20- and the 30-mode, respectively. All three microbridges show similar displacement amplitude values, whereas the deviation between those three are most likely due to manufacturing uncertainties. The 20-mode has its maximum at the buckling point, whereas for the 30-mode the amplitude increases with decreasing strain values, reaching its maximum in the buckling regime at -0.2 mm m^{-1}.

Fig. 12 (c) and (d) show the same modes for all three microbridges measured with the IA. As expected, devices with higher widths show higher conductance peaks, due to the larger area what in turn leads to a higher amount of generated polarization charges, when the microbridge is resonating.

4.5. Gauge factor

For resistive strain gauges the dimensionless gauge factor $k_{resistive}$ is defined as the slope of the normalized resistance depending on ε and is calculated according to
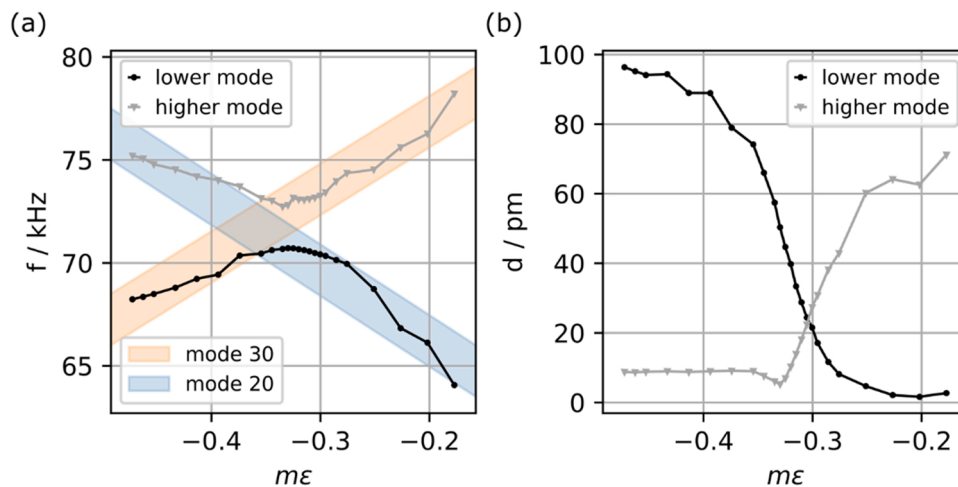

Fig. 10. (a) Shift of resonance frequency as a function of strain for the 20- and the 30-mode of a microbridge around the buckling point, clearly showing the avoided crossing phenomenon. The blue and orange marks indicate how the modes would behave without the veering effect. (b) The corresponding displacements of the 20- and the 30-mode.
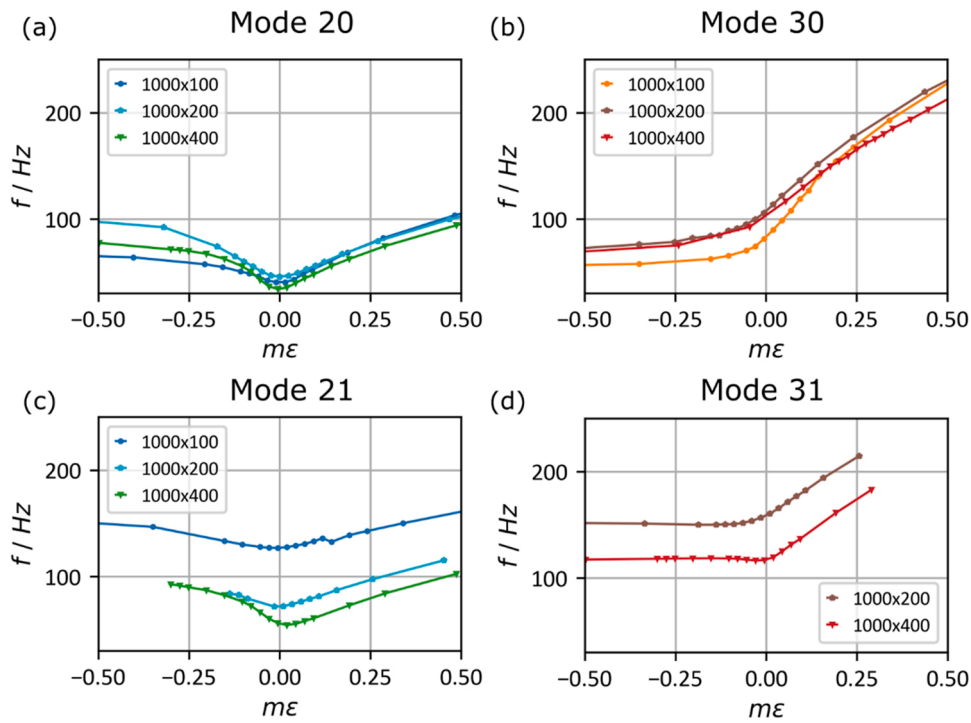
Fig. 11. Resonance frequencies as a function of applied strain for the 20-mode (a), the 30-mode (b), the 21-mode (c) and the 31-mode (d) whereas the 31-mode for the microbridge with a width of 100 μm could not be measured due to the weak signal strength.
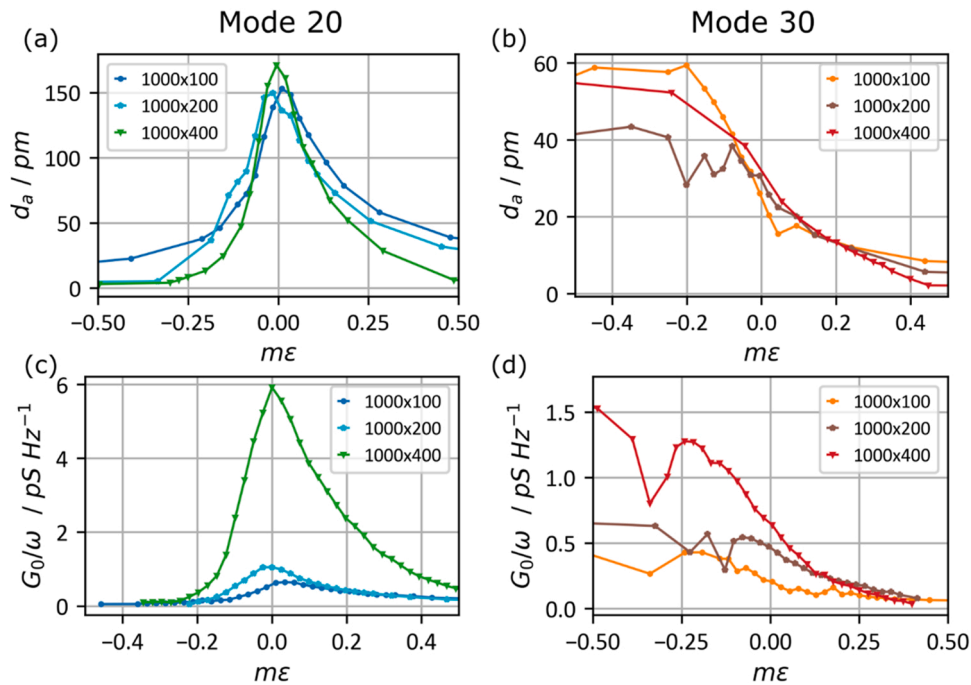

Fig. 12. Averaged displacement d_a and conductance peak height G_0/ω as a function of strain for the 20-mode in (a) and (c), and for the 30-mode in (b) and (d).

$$k_{resistive} = \frac{\Delta R / R_0}{\varepsilon} \qquad (10)$$

where ΔR is the change in resistance for a given strain ε and R_0 is the resistance at $\varepsilon = 0$. Similar, a dimensionless gauge factor for resonant strain sensors $k_{resonant}$ can be defined with

$$k_{resonant} = \frac{\Delta f / f_0}{\varepsilon} \qquad (11)$$

where Δf is the change in resonance frequency for a given strain ε and $f_0 = f(\varepsilon)$ is the resonance frequency in the defined reference point. Due to the non-linear behavior of $f(\varepsilon)$ and reasons given in previous sections, the definition of a working point is important. Fig. 13 (a) shows the gauge factors for the even modes 20, 40 and 60 and in Fig. 13 (b) are the odd modes 30, 50 and 70. In the non-buckling regime all modes show positive values for the gauge factor, with very high values of up to 3500. In the buckling regime, even modes show negative gauge factors with
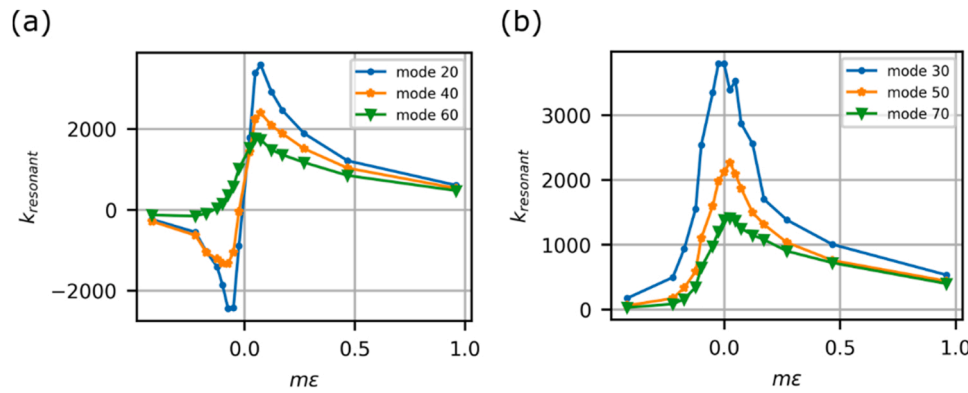
Fig. 13. Gauge factor as a function of strain for (a) the even modes 20, 40 and 60 and (b) the uneven modes 30, 50 and 70.

slightly reduced values, whereas the gauge factors for odd modes almost vanish. Lower order modes have a higher gauge factor than higher order modes making them the better choice for an application as strain sensor.

Although such high gauge factors were predicted for resonant strain sensors with finite element simulations [56], most previous experimental work only reached gauge factors of up to 500 (see Table 3), making our device approximately one order of magnitude more responsive than most of the current state-of-the-art. Even compared to other types of strain sensors (see Table 4) e.g., piezoresistive materials like carbon nanotubes or strain sensors based on the spintronic technology, our sensor shows a competitive gauge factor.

Obviously, if operated as a strain sensor the device has to be operated in a reference point, so that if negative strain is applied the sensor does not change its buckling regime, as the gauge factor changes its sign and it would not be possible to distinguish positive from negative strain values. The smaller the range of possible applied strain, the closer the working point can be set to the buckling point, which results in higher gauge factors.

This working point can be set by pre-straining the sensor before or during the mounting process of the sensor. In the featured measurement-setup the cantilever beam was bent upwards before the sensor was glued onto its surface. The subsequent release into the cantilevers zero position acts as a pre-straining moving its buckling point to the left in Fig. 4. In a real-world application this pre-straining process is difficult to achieve as it is not often possible to pre-bend the surface of the test object. In this case the pre-straining can be done during the packaging process which must be done anyway to protect the sensor from damage.

Table 3
State-of-the-art piezoelectric and capacitive resonant strain sensors.

Type	Material	Gauge Factor	Sensitivity $Hz\mu m^{-1}$	Strain Range %	Year	Ref.
Res. Piezo. MEMS	Si/AlN	3500	n.A.	±0.1	2022	This Work
Res. Piezo. MEMS	Si/AlN	2510	150	n.A.	2017	[30]
Res. Piezo. MEMS	Si/AlN	244	243	0.037	1996	[32]
Res. Cap. MEMS	Si	539	164	0.063	2016	[57]
Res. Cap. MEMS	Si	15	2.8	0.1	2016	[31]
Res. Cap. MEMS	SiC	128	41.7	0.005	2019	[58]
Res. Cap. MEMS	Si	97	20.8	0.063-	2011	[59]

Table 4
Piezoresistive, metallic and other types of strain sensors.

Type	Material	Gauge Factor	Strain Range %.	Year	Ref.
Capacitive MEMS	Si	430	0.1%	2021	[60]
Piezoresistive	Si	155	n.A.	1953	[61]
Piezoresistive	Ge	100	0.04%	1969	[62]
Piezoresistive	B-Doped SiC Nanobelts	-1800	n.A.	2020	[63]
Piezoresistive	Carbon Nanotubes	2900	0.4%	2006	[64]
Spintronic	Co-Fe-B RL/Mg-O BL/FE-B	5072	±0.1%	2017	[65]
Metallic	Pt/AlN	5		2020	[66]
Metallic	Zr	3.4	1%	2020	[67]
Metallic	Cu	1.4	1%	2020	[67]
Metallic	Ni	-12.2	n.A.	1967	[68]

5. Conclusion

In this work we presented a piezoelectric resonant MEMS strain sensor based on a microbridge structure. The sensor devices have been measured optically, by using a laser Doppler vibrometer to analyze the mode shapes and mechanical displacements. The electric conductance spectra of the structures have been studied with an impedance analyzer, which gives the opportunity for a pure electrical read out.

Both measurement techniques have been used to study the 20- and 30-mode in detail over a strain range of $-1m\varepsilon$ to $1m\varepsilon$ around the critical strain value ε_c. It could be observed that in the buckling regime the mode shapes get distorted, which affects the displacement and the conductance spectra differently, depending on the mode number. Another effect which could be measured is the mode veering effect, which explains why the modes do not cross, but rather exchange their mode shapes, which leads to additional non-linear behavior around those veering areas, giving additional challenges during the read out.

Furthermore, several sensor devices with varying width (100, 200 and 400 μm) have been manufactured. It shows that wider microbridges provide a up to 10 times higher conductance peak, which makes the electrical read out straightforward. At the same time a larger number of higher order modes appear at lower frequencies of their specific spectra making it more difficult to distinguish between those modes.

A gauge factor for resonant strain sensors could be determined, resulting in an up to 1000 times higher gauge factor than conventional resistive strain sensors and a 10 times higher GF than current state-of-the-art resonant strain sensors. Combined with an all-electric read out and the possibility to realize very low power devices, this piezoelectric sensor provides a promising option for future strain sensing applications.

CRediT authorship contribution statement

M. Schlögl: Conceptualization, Methodology, Software, Formal analysis, Investigation, Writing – original draft, Visualization. **S. Köpl:** Formal analysis, Investigation. **J. Hiesberger:** Formal analysis, Investigation. **M. Schneider:** Conceptualization, Methodology, Resources, Writing – review & editing, Supervision. **U. Schmidt:** Conceptualization, Resources, Writing – review & editing, Funding acquisition, Project administration, Supervision.

Declaration of Competing Interest

The authors declare that they have no known competing financial interests or personal relationships that could have appeared to influence the work reported in this paper.

Data Availability

Data will be made available on request.

Acknowledgments

References

[1] L.E. Aygun, V. Kumar, C. Weaver, M. Gerber, S. Wagner, N. Verma, B. Glisic, J. C. Sturm, Sensors 20 (2020) 1386.
[2] T.J. Arsenault, A. Achuthan, P. Marzocca, C. Grappasonni, G. Coppotelli, Smart Mater. Struct. 22 (2013), 075027.
[3] X. Hu, B. Wang, H. Ji, Comput. Aided Civ. Infrastruct. Eng. 28 (2013) 193–209.
[4] L. Massari, C.M. Oddo, E. Sinibaldi, R. Detry, J. Bowkett, K.C. Carpenter, Front. Neurorobotics 13 (2019) 8.
[5] J. Oh, J.C. Yang, J.-O. Kim, H. Park, S.Y. Kwon, S. Lee, J.Y. Sim, H.W. Oh, J. Kim, S. Park, ACS Nano 12 (2018) 7546–7553.
[6] Z. Pei, Q. Zhang, K. Yang, Z. Yuan, W. Zhang, S. Sang, Adv. Mater. Technol. 6 (2021) 2100038.
[7] J. Tolvanen, J. Hannu, H. Jantunen, Sci. Rep. 8 (2018) 13241.
[8] W.A.D.M. Jayathilaka, K. Qi, Y. Qin, A. Chinnappan, W. Serrano-García, C. Baskar, H. Wang, J. He, S. Cui, S.W. Thomas, S. Ramakrishna, Adv. Mater. 31 (2019) 1805921.
[9] Y. Li, Y.A. Samad, T. Taha, G. Cai, S.-Y. Fu, K. Liao, ACS Sustain. Chem. Eng. 4 (2016) 4288–4295.
[10] P.K. Stein, Exp. Tech. 14 (1990) 13–19.
[11] A.C. Ruge, Strain Gauge, US2350972A, 1944.
[12] A. Maskay, M. Pereira da Cunha, Sens. Actuators Phys. 259 (2017) 34–43.
[13] K.E. Wojciechowski, B.E. Boser, A.P. Pisano, in: Proceedings of the 17th IEEE International Conference on Micro Electro Mechanical Systems: Maastricht: MEMS 2004 Technical Digest, 2004, pp. 841–845.
[14] D.J. Lichtenwalner, A.E. Hydrick, A.I. Kingon, Sens. Actuators Phys. 135 (2007) 593–597.
[15] V. Yokaribas, P. Kraemer, A.B. Mende, J. Ruhkopf, M.C. Lemme, C.-P. Fritzen, Small Sci. n/a (n.d.) 2100088.
[16] J. Shen, T. Wang, Y. Luo, X. Zeng, C. Cao, Optik 178 (2019) 794–801.
[17] A.S. Fiorillo, C.D. Critello, S.A. Pullano, Sens. Actuators Phys. 281 (2018) 156–175.
[18] P. Song, G. Wang, Y. Zhang, Sens. Actuators Phys. 323 (2021), 112659.
[19] P. Moyo, J.M.W. Brownjohn, R. Suresh, S.C. Tjin, Eng. Struct. 27 (2005) 1828–1834.
[20] H.-E. Joe, H. Yun, S.-H. Jo, M.B.G. Jun, B.-K. Min, Int. J. Precis. Eng. Manuf. Green. Technol. 5 (2018) 173–191.
[21] F.M. Sánchez-Arévalo, G. Pulos, Mater. Charact. 59 (2008) 1572–1579.
[22] J. Sirohi, M.S. Lawson, Opt. Eng. 51 (2012), 043603.
[23] S. Li, X. Li, Y. Qin, Y. Zhao, Micro Nano Lett. 15 (2020) 1028–1032.
[24] J.G. Njiri, N. Beganovic, M.H. Do, D. Söffker, Renew. Energy 131 (2019) 818–828.
[25] E. Weymar, M. Finkbeiner, Int. J. Life Cycle Assess. 21 (2016) 215–223.
[26] D. Platz, U. Schmid, J. Micromech. Microeng. 29 (2019), 123001.
[27] G. Pfusterschmied, M. Kucera, W. Steindl, T. Manzaneque, V. Ruiz Díez, A. Bittner, M. Schneider, J.L. Sánchez-Rojas, U. Schmid, Sens. Actuators B Chem. 237 (2016) 999–1006.
[28] M. Schneider, G. Pfusterschmied, F. Patocka, U. Schmid, E Elektrotech. Inf. 137 (2020) 121–127.
[29] F. Patocka, M. Schneider, N. Dörr, C. Schneidhofer, U. Schmid, J. Micromech. Microeng. 29 (2019), 045009.
[30] S. Ghosh, J.E.-Y. Lee, IEEE Sens. (2017) 1–3.
[31] C.D. Do, A. Erbes, J. Yan, K. Soga, A.A. Seshia, J. Microelectromech. Syst. 25 (2016) 851–858.
[32] F.T. Goericke, M.W. Chan, G. Vigevani, I. Izyumin, B.E. Boser, A.P. Pisano, in: Proceedings of the 16th International Solid-State Sensors, Actuators and Microsystems Conference, 2011, pp. 1994–1997.
[33] R.G. Azevedo, D.G. Jones, A.V. Jog, B. Jamshidi, D.R. Myers, L. Chen, X. Fu, M. Mehregany, M.B.J. Wijesundara, A.P. Pisano, IEEE Sens. J. 7 (2007) 568–576.
[34] M. Suster, J. Guo, N. Chaimanonart, W.H. Ko, D.J. Young, J. Microelectromech. Syst. 15 (2006) 1069–1077.
[35] S. Schmid, L.G. Villanueva, M.L. Roukes, Fundamentals of Nanomechanical Resonators, Springer International Publishing, Cham, 2016.
[36] O.A. Bauchau, J.I. Craig, in: O.A. Bauchau, J.I. Craig (Eds.), Structural Analysis, Springer, Dordrecht, Netherlands, 2009, pp. 173–221.
[37] C. Gui, R. Legtenberg, H.A.C. Tilmans, J.H.J. Fluitman, M. Elwenspoek, J. Microelectromech. Syst. 7 (1998) 122–127.
[38] S. Bouwstra, B. Geijselaers, in: Proceedings of the International Conference on Solid-State Sensors and Actuators: Digest of Technical Papers, Transducers, 1991, pp. 538–542.
[39] A.R. Behera, H. Shaik, G.M. Rao, R. Pratap, J. Microelectromech. Syst. 28 (2019) 1039–1054.
[40] X. Song, H. Liu, American Society of Mechanical Engineers Digital Collection, 2020.
[41] H. Wang, X. Ning, H. Li, H. Luan, Y. Xue, X. Yu, Z. Fan, L. Li, J.A. Rogers, Y. Zhang, Y. Huang, J. Mech. Phys. Solids 112 (2018) 187–208.
[42] A.H. Nayfeh, W. Kreider, T.J. Anderson, AIAA J., 2012.
[43] P. Majda, J. Skrodzewicz, Int. J. Adhes. Adhes. 29 (2009) 396–404.
[44] M. Dolz, M.J. Hernández, J. Delegido, Food Hydrocoll. 22 (2008) 421–427.
[45] L. Belsito, M. Ferri, A. Roncaglia, in: Proceedings of the 20th International Conference on Solid-State Sensors, Actuators and Microsystems, Transducers Eurosensors XXXIII, 2019, pp. 2009–2012.
[46] B.D. Sosnowchik, R.G. Azevedo, D.R. Myers, M.W. Chan, A.P. Pisano, L. Lin, J. Microelectromech. Syst. 21 (2012) 497–506.
[47] A.W. Leissa, Z. Angew. Math. Phys. ZAMP 25 (1974) 99–111.
[48] R.W. Claassen, C.J. Thorne, J. Aerosp. Sci. 29 (1962) 1300–1305.
[49] A.Z. Hajjaj, N. Alcheikh, M.I. Younis, Int. J. Non-Linear Mech. 95 (2017) 277–286.
[50] N. Alcheikh, A.Z. Hajjaj, M.I. Younis, Sens. Actuators Phys. 300 (2019), 111652.
[51] N. Alcheikh, H.M. Ouakad, S.B. Mbarek, M.I. Younis, J. Microelectromech. Syst. (2021) 1–13.
[52] N. Alcheikh, S.B. Mbarek, S. Amara, M.I. Younis, IEEE Sens. J. 21 (2021) 13165–13175.
[53] T. Rabenimanana, V. Walter, N. Kacem, P. Le Moal, G. Bourbon, J. Lardiès, Sens. Actuators Phys. 295 (2019) 643–652.
[54] V. Pachkawade, IEEE Sens. J. 21 (2021) 8751–8779.
[55] M. Schneider, A. Bittner, U. Schmid, Appl. Phys. Lett. 105 (2014), 201912.
[56] S.P. Beeby, G. Ensell, B.R. Baker, M.J. Tudor, N.M. White, J. Microelectromech. Syst. 9 (2000) 104–111.
[57] L. Belsito, M. Ferri, F. Mancarella, L. Masini, J. Yan, A.A. Seshia, K. Soga, A. Roncaglia, Sens. Actuators Phys. 239 (2016) 90–101.
[58] L. Belsito, M. Bosi, F. Mancarella, M. Ferri, A. Roncaglia, J. Microelectromech. Syst. 29 (2020) 117–128.
[59] M.W. Chan, D.R. Myers, B.D. Sosnowchik, L. Lin, A.P. Pisano, in: Proceedings of the 16th International Solid-State Sensors, Actuators and Microsystems Conference, 2011, pp. 2859–2862.
[60] C. Zhang, S.-Y. Zhang, L.-F. Wang, IEEE Sens. J. 21 (2021) 22527–22535.
[61] C.S. Smith, Phys. Rev. 94 (1954) 42–49.
[62] W.D. Edwards, R.P. Beaulieu, J. Phys. [E] 2 (1969) 613–615.
[63] X. Li, F. Gao, L. Wang, S. Chen, B. Deng, L. Chen, C.-H. Lin, W. Yang, T. Wu, ACS Appl. Mater. Interfaces 12 (2020) 47848–47853.
[64] C. Stampfer, A. Jungen, R. Linderman, D. Obergfell, S. Roth, C. Hierold, Nano Lett. 6 (2006) 1449–1453.
[65] Y. Fuji, M. Hara, Y. Higashi, S. Kaji, K. Masunishi, T. Nagata, A. Yuzawa, K. Otsu, K. Okamoto, S. Baba, T. Ono, A. Hori, H. Fukuzawa, in: Proceedings of the 19th International Conference on Solid-State Sensors, Actuators and Microsystems, Transducers, 2017, pp. 63–66.
[66] Sens. Actuators Phys., 302, 2020, 111805.
[67] Y.-C. Lu, C.-Y. Chiang, Y.-C. Chen, Y.-C. Lin, T. Ono, Y.-C. Tsai, Jpn. J. Appl. Phys. 59 (2020) SIIG10.
[68] M.L. Meyer, J. Strain Anal. 2 (1967) 324–331.

M. Schlögl received his Bachelor and master's degree in electrical engineering from TU Wien in 2015 and 2018, respectively. He is currently working on his Ph.D. thesis on materials and devices for piezoelectric energy harvesting and resonant strain sensing at the Department of Microsystems Technology at TU Wien.

S. Köpl studied electrical engineering at TU Wien and received his bachelor's degree in 2021. During his bachelor's thesis he worked on resonant piezoelectric microbridges for strain sensing.

J. Hiesberger studied electrical engineering at TU Wien and received his bachelor's degree in 2021. Currently he is working on a master's degree in Embedded Systems at TU Wien. Parallel he is working as an assistant at the Institute of Sensor and Actuator Systems and collects practical lab experience.

M. Schneider studied physics at the Karlsruhe Institute of Technology 2003–2009. He performed his diploma work at the Forschungszentrum Karlsruhe on the measurement of Lorentz angles in highly irradiated silicon strip detectors for high energy collider

applications such as the large hadron collider at CERN. He finished his studies in 2009 and started his Ph.D. thesis on the optimization of ultra-thin aluminum nitride films for actuation and sensing applications at the Department of Microsystems Technology at TU Wien. He received his Ph.D. in 2014 and is currently working as assistant professor on the topic of advanced piezoelectric microsystems.

U. Schmid started studies in physics and mathematics in 1992. He performed his diploma work at the research laboratories of the Daimler–Benz AG on the electrical characterization of silicon carbide microelectronic devices for high temperature applications. In 1999, he joined the research laboratories of Daimler–Chrysler AG (now Airbus Group) in Ottobrunn/Munich. He developed a robust fuel injection rate sensor for automotive diesel engines and received his Ph.D. degree in 2003. From 2003–2008, he was a post-doc at the Chair of Micromechanics, Microfluidics/Microactuators at Saarland University. Since October 2008, he is a full professor for Microsystems Technology at TU Wien.